LA-UR- 10-01242

Approved for public release;
distribution is unlimited.

Title:	MULTI-SOURCE ENERGY HARVESTER TO POWER SENSING HARDWARE ON ROTATING STRUCTURES
Author(s):	Alexander D. Schlichting, LANL, INST-OFF Scott Ouellette, LANL, INST-OFF Clinton P. Carlson, LANL, INST-OFF Kevin Farinholt, LANL, AET-1 Gyuhae Park, LANL, INST-OFF Charles Farrar, LANL, INST-OFF
Intended for:	SPIE - Smart Materials and Structures & Nondestructive Evaluation Symposium

Los Alamos
NATIONAL LABORATORY
EST. 1943

Form 836 (7/06)

Multi-Source Energy Harvester to Power Sensing Hardware on Rotating Structures

Alexander Schlichting[1], Scott Oullette[2], Clinton Carlson[3],
Kevin M. Farinholt[4], Gyuhae Park[5], Charles R. Farrar[5]

[1]Department of Mechanical and Aerospace Engineering, Cornell University
[2]Department of Structural Engineering, University of California – San Diego
[3]Department of Civil Engineering, University of Michigan
[4]AET-1, MS-H821, Los Alamos National Laboratory, Los Alamos, NM 87545
[5]The Engineering Institute, MS-T001, Los Alamos National Laboratory, Los Alamos, NM 87545

ABSTRACT

The U.S. Department of Energy (DOE) proposes to meet 20% of the nation's energy needs through wind power by the year 2030. To accomplish this goal, the industry will need to produce larger (>100m diameter) turbines to increase efficiency and maximize energy production. It will be imperative to instrument the large composite structures with onboard sensing to provide structural health monitoring capabilities to understand the global response and integrity of these systems as they age. A critical component in the deployment of such a system will be a robust power source that can operate for the lifespan of the wind turbine. In this paper we consider the use of discrete, localized power sources that derive energy from the ambient (solar, thermal) or operational (kinetic) environment. This approach will rely on a multi-source configuration that scavenges energy from photovoltaic and piezoelectric transducers. Each harvester is first characterized individually in the laboratory and then they are combined through a multi-source power conditioner that is designed to combine the output of each harvester in series to power a small wireless sensor node that has active-sensing capabilities. The advantages/disadvantages of each approach are discussed, along with the proposed design for a field ready energy harvester that will be deployed on a small-scale 19.8m diameter wind turbine.

1. INTRODUCTION

Global climate change has sparked renewed interest in domestic and renewable energy sources in the United States for both economic and environmental reasons. In 2008, the U.S. wind energy industry brought online over 8,500 megawatts (MW) of new wind power capacity, increasing the nation's cumulative total by 50% to over 23,000 MW – accounting for 1.5% of the total energy produced - and pushing the U.S. above Germany as the country with the largest amount of installed wind power capacity.[1] Currently, the U.S. has approximately 15,000 - 20,000 wind turbines in operation across 34 states. The largest wind farm in the U.S. is located in Taylor, Texas, where 421 wind turbines produce 735 MW of electric capacity. On average, wind farms cost $1 million per megawatt of installed capacity, and the annual maintenance cost for each wind turbine is approximately 1.5% - 2% of the original cost.[2, 3] With the U.S. looking to expand wind energy to account for 20% of the total energy output by 2030, the ability to transition from time-based maintenance to condition-based maintenance could potentially cut maintenance costs by 50%, resulting in a cost savings of approximately $2 - 3 billion dollars annually.

At present, turbine designs used in the U.S. follow European design criterion, which fail to meet the more severe loading conditions observed in the wind corridor of the Midwestern states. In addition, wind turbine blade lengths continue to grow (>50m) in an effort to capture more of the inbound wind energy. As such, unforeseen structural failures due to the complex loading along the length of the blade plague the industry. Also, in order to reduce the weight while still maintaining the necessary strength and stiffness characteristics, manufacturers use composite materials (e.g. fiberglass or carbon-fiber) to construct the blades (Figure 2). However, significant drawbacks exist from the manufacturing process as blades may possess material flaws such as voids in the epoxy, delamination, and surface wrinkles. Under sufficient loading these flaws grow and in some cases endanger the structural integrity of the blade and by extension the entire turbine as well.

Table 1: Current and Power Draw for WID 3.0[5]

Mode	Current (mA)	Power (mW)
Measurement	26	72.8
Data Transmission	22	61.6
Sleep Mode	0.075	0.21

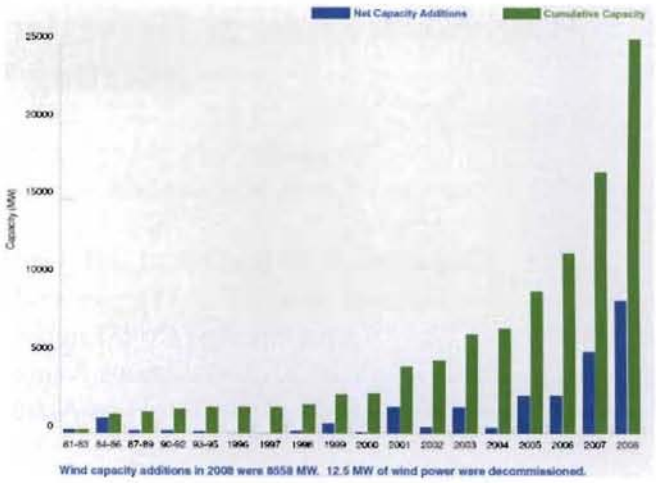

Figure 1: U.S. wind turbine growth[1]

The Structural Health Monitoring (SHM) process presents a possible solution to this issue. During this process, sensors embedded in the structure of the blade at critical locations actively monitor the structure for damage. Refer to the report from the Energy Harvesting for Structural Health Monitoring Sensor Networks workshop held at Los Alamos National Laboratory for a brief introduction to the SHM process.[4] Wind turbine blades present multiple implementation challenges due to the overall design of the wind turbine. An SHM sensor network with wires running along the length of the blades increases the turbine's vulnerability to lightning as it would create multiple conductive paths in addition to the existing lightning protection system already embedded in the blade. Therefore, any sensor network must rely on wireless technology in order to extract data from the sensor nodes. Also, the rotating hub of the wind turbine requires a decentralized active sensing and processing network with a hybrid design as detailed in Park et al. (2005). Since the sensor nodes themselves will be dispersed along the length of the blade, and wired power is impractical due to lightning issues, a long-term power management system must be implemented, with energy harvesting serving as one possible solution to this problem.

This research focuses on the overall goal of reducing maintenance costs by investigating various energy harvesting methods on a wind turbine blade to power the wireless sensor nodes. The node under consideration in this research is the wireless impedance device (WID) developed at Los Alamos National Laboratory. The WID is designed specifically to operate with different power sources, ranging from batteries to energy harvesting sources to wireless energy transmission methods. Under normal operation the WID cycles through several different operating modes, including a measurement cycle, a data transmission cycle and a sleep cycle. The power requirements for each state are presented in Table 1. For energy harvesting sources the sensor node has an onboard power conditioning module that limits the power released to the system's onboard microcontroller to between 2.7V–3.5V, the stable operating range of the WID.[5]

2. ENERGY HARVESTING METHODS

Of the common energy harvesting methods, the three most common sources considered in this investigation were ambient vibrations, thermal energy and solar energy. Initial tests indicated a maximum thermal gradient of ~10°C across the thickness of a CX-100 blade section during a sunny summer day in Los Alamos; this is insufficient to generate the amount of energy necessary to power the WID sensor node using existing thermoelectric modules. Therefore, the two methods discussed in this paper will include vibration energy harvesting using piezoelectric materials, and solar energy harvesting using photovoltaic cells.

2.1 Vibration Energy Harvesting with Piezoelectric Materials

Piezoelectric materials belong to the family of ferroelectric materials whose molecular structure consists of electric dipoles. The piezoelectric effect states that when a mechanical strain is present in the material a potential difference is created across the dipoles. This behavior allows piezoelectric materials to be used as sensors or actuators as well as for energy harvesting purposes. For manufactured materials, the piezoelectric effect appears in the presence of a strong electric field while the material undergoes heating.

Figure 2: CX-100 Cross Section

One material that exhibits a strong piezoelectric effect, or electromechanical coupling, is lead zirconate titanate (PZT). PZT sensors typically come in stack and patch configurations. In the stack configuration both the electrical field and the mechanical strain act in the same direction, the "3" direction. In the patch, or bender, configuration, the electrical field and the mechanical strain act in different directions, the "3" and the "1" direction. Therefore a stack configuration operates in the "33" mode and a bender operates in the "31" mode. Note that the poling for both configurations acts in the "3" direction, which by convention will always be the case. This naming convention mainly comes into play when referring to the electromechanical coupling coefficients for actuation, "d", and for sensing, "g". For example, an electromechanical coupling coefficient labeled "g_{31}" describes a piezoelectric sensor in the bending configuration.[8]

Each configuration has its own advantages and common applications. The stack configuration displays large electromechanical coupling coefficients but small deflections, limiting its use primarily to actuation applications which require large forces. The bender configuration amplifies the deflection of the material due to its geometry, making it ideal for energy harvesting from vibration or actuation applications which require larger deflections than the stack configuration can provide.

Testing on piezoelectric materials has shown that they possess a very large bandwidth of operation. Piezoelectric materials also have no moving parts, so they produce little noise and have low maintenance requirements. However, piezoelectric materials only undergo small displacements and, in turn, produce lower power outputs compared to other materials used in energy harvesting. Tests have shown that piezoelectric-based energy harvesters are capable of producing approximately 800 $\mu W/cm^3$ when mounted to machines that vibrate in the kHz range.[9]

2.2 Solar Energy Harvesting with Photovoltaic (PV) Cells

Photovoltaic cells consist of semiconductor materials such as crystalline silicon as well as single and polycrystalline thin films. Similar to thermoelectric modules, p-type and n-type materials are separated by a junction. When solar radiation energizes the molecules of the materials, a current is formed over the junction due to the differences the p-type materials having an abundance of "holes" where electrons could go and the n-type materials having an abundance of electrons.[10]

Two main system configurations have arisen during the technology's short lifespan, flat plate systems and concentrator systems. The flat plate system arranges the photovoltaic cells on a flat surface with a simple plastic or glass cover. Sometimes a tracking system angles the array so that the maximum amount of solar energy is collected at all times of the day. The concentrator system instead minimizes the amount of photovoltaic material needed by concentrating the solar radiation using plastic lenses and metal reflective housings. This system is more powerful than the flat plate system and operates at a much higher efficiency when it is exposed to concentrated light. However the drawbacks include, but are not limited to, cost, the risk of overheating and requiring a tracking system for optimal output throughout the day. Photovoltaic materials have produced 100 $\mu W/cm^2$ in common settings and a much larger 100 mW/cm^2 in direct sunlight during testing.[9]

2.3 MISO Power Management Circuit

With multiple sources of energy available on a wind turbine blade, each of which produces unique electrical energy characteristics, combining multiple energy sources to power a single sensor node is necessary in order to offset operational and environmental variability. The power management circuit (Figure 3) is designed to sort a dynamic

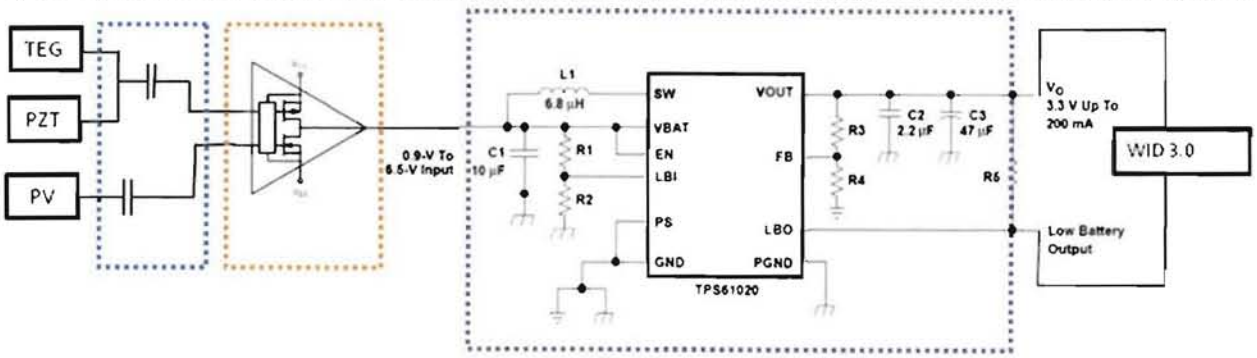

Figure 3: MISO Power Management Circuit

Figure 4: Experimental setups of the cantilever, the cantilever with lumped mass and the L-shaped bracket.

voltage range (0.9-6.5V) from multiple energy harvesting modules and provide DC voltage compliance (2.7-3.5V) to the WID 3.0 sensor node. The circuit is a three-stage multiple-input single-output (MISO) system.

- Stage 1 – highlighted in blue – stores the energy into two 1F super capacitors. The voltage output from TEG and PZT modules are relatively low compared to the PV module. In addition, the PZT module produces an AC voltage output, and therefore needs AC-DC rectification prior to charging the capacitor.
- Stage 2 – highlighted in orange – dynamically compares the voltage stored on each capacitor and passes the larger voltage. The comparator used has an operational voltage range of 0.85-6V.
    - *Note:* dynamic sorting means the highest reference voltage is continuously monitored due to the fact that energy harvesting modules are subject to operational and environmental variability. For example, a photovoltaic module might perform slightly better than a TEG module due to direct sunlight low thermal gradient; however, at night, the TEG might perform better due to residual heat and good insulation.
- Stage 3 – highlighted in violet – is a buck/boost converter that accepts voltages in the range of 0.9-6.5V. The converter can be customized for variable output voltages. The diagram shown in Figure 3 is designed for 3.3V and up to 200mA, which is compliant with the WID 3.0 power requirements.

3. EXPERIMENTAL SETUP

3.1 Piezoelectric Testing

In order to determine the power production of piezoelectric materials on the wind turbine blade, a previously studied L-shaped bracket is explored (Figure 4). This configuration possesses advantages over the standard cantilevered beam due to its two-to-one internal resonance. Instead of a theoretical ratio of 6.27 between the first and second resonance frequencies as with a cantilever without a lumped mass at the tip, the L-shaped bracket can obtain a ratio as low as 2. This presents an advantage when attempting to harvest energy from ambient vibrations because the frequency of vibration does not remain constant but travels across a small range. Therefore tuning the L-shaped bracket so that the frequencies of the ambient vibrations lie between the first two modes will produce more power from the piezoelectric materials than with a cantilever energy harvester.[11]

As Erturk et al.[11] stopped at an analytical model of the system, this work focuses on a finite element modal analysis of the base structure without the piezoelectric material as well as an experimental L-shaped bracket with piezoceramic patches on the beams. Stainless steel beams, polycarbonate lumped masses of 48.2 and 28.3 grams, and 5A4E PZT piezoceramic patches were used in the experimental setup (see Table 2 for parameters). The finite element modal analysis was performed on ABAQUS CAE with both beam and shell elements. The experimental testing consisted of modal analyses as well as capacitor charging tests on an electromagnetic shaker for a simple cantilever beam, a cantilever beam with a proof-mass at the tip and the L-shaped bracket.

Table 2: L-Shaped bracket parameters

	Length (cm)	Width (cm)	Thickness (mm)
Horizontal Beam	21.1	3.8	0.79
Vertical Beam	35.6	2.5	0.79
Lumped Mass 1	5.7	2.5	25.4
Lumped Mass 2	5.7	1.9	25.4
PZT Patch 1	3.8	3.2	0.27
PZT Patch 2	3.8	2.5	0.27

3.2 Photovoltaic Testing

The photovoltaic testing involved five different photovoltaic cells from the PowerFilm line (Table 3).. The experimental setup consisted of the photovoltaic cells taped down to a single composite flat surface (Figure 7). The goal of the tests pertained to the effect of cell temperature, solar radiation level, composite substrate temperature, and solar incidence angle on the power output of the cells. The power output of the cells was calculated by measuring the potential difference across the leads as well as the current output of the cells. In order to test the effects of the cell temperature and the composite substrate on power output, the experimental setup was placed outside on a sunny day. An infrared thermometer measured the temperature of each individual cell in the five photovoltaic arrays and a thermocouple attached to the composite substrate surface measured the temperature of the photovoltaic cell's base. Also, charging tests with various capacitors explored the ability of the cells to charge a capacitor that could be used to power the WID 3.0 sensor node.

Table 3: Specifications for the PowerFilm photovoltaic cells.

Model	Size (l x w x h, in.)	Operating Voltage (V)	Operating Current (mA)	Weight (oz.)
S-MPT3.6-75	2.9 x 3.0 x 0.01	3.6	50	0.06
S-MPT3.6-150	2.9 x 5.9 x 0.01	3.6	100	0.10
S-MPT4.8-75	3.7 x 3.0 x 0.01	4.8	50	0.07
S-MPT4.8-150	3.7 x 5.9 x 0.01	4.8	100	0.10
S-MPT6-75	4.5 x 3.0 x 0.01	6.0	50	0.08

The tests examining the effect of the solar incidence angle on the photovoltaic cell output utilized six different angles: 0°, 10°, 13°, 19°, 30° and 46° (Figure 8). Single point measurements of the voltage, current, and alignment angle of the experimental setup in the north-south direction eliminated the effect of the changing position of the sun during each of the tests. The effects of solar radiation on the power of the cells were tested by placing the cells in various lighting conditions. The experiment consisted of measuring the voltage and current output of the photovoltaic cells while placing the setup in direct sunlight on a flat surface and at a 43° solar incidence angle, a shaded area outside, a box with holes to allow sunlight through (Figure 9) and a lab with fluorescent lighting. The solar radiation could not be directly calculated in the different environments, but as the level of exposure to actual sunlight increases the solar radiation should as well.

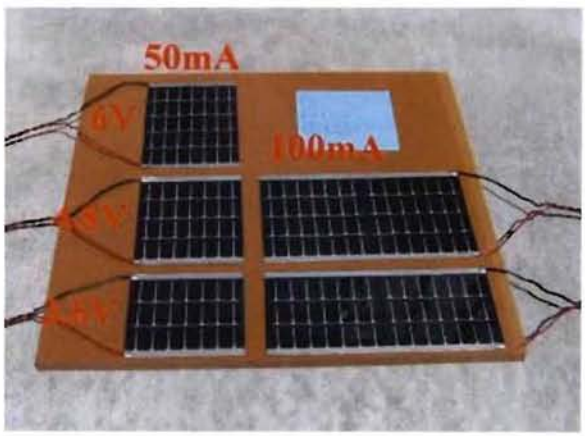

Figure 7: Photovoltaic cells experimental setup

For the capacitor charging tests, the capacitor was tied to the leads of one cell and grounded while a Dactron program recorded the voltage of the capacitor over a set time period. After the program initially started recording data, the ground was removed from the capacitor and the capacitor began charging. The energy (E) was calculated using

$$E = \frac{1}{2} C V^2 \qquad (2)$$

where V is the measured voltage and C is the capacitance of the capacitor in the circuit. Normalizing the energy with respect to the area of the cells produced a truer representation of how well the cells performed. The slope of a linear fit of the energy density curve provided the power density of the cells. Three capacitors were initially tested, but a 0.1F 5V capacitor charged too fast and a 4.7F 2.5V capacitor did not charge enough, so they were removed from

Figure 8: Incidence angle tests

further testing. Therefore subsequent tests used only a 2.2F 2.5V capacitor.

In a follow-up test, a 1F 5V capacitor was charged using the same connections and procedure as the initial charging tests, but in two different conditions: solar incidence angles of 0° and 33°. The voltages, energy densities and power densities were calculated using the same methods as the 2.2F capacitor charging test. However, for this test, the average power density was calculated for each condition. The average power density for the 33° angle was subtracted from the average power density for the 0° angle to produce a difference plot to show the variation in the power density between the different conditions (Figure 25). The purpose of this test was to see what effects, if any, a less than optimal condition had on the charging of a capacitor.

Figure 9: Low Radiation Experimental Test Setup

3.3 Boost Converter Testing

The boost converter (Figure 10) tested was the Texas Instruments TPS61020; a low-power synchronous booster IC with input voltage range of 0.9V to 6.5V. The output voltage is adjustable by the voltage dividers on the output pin, and - for these tests - was 3.3V. The internal synchronous rectifier and the capacitors on the output voltage pin control the voltage ripple. The boost converter was soldered to a 72-pin Schmartboard with a 0.5mm pitch to match the surface-mount pin connections on the TPS61020. Wire leads were then soldered to the Schmartboard in order to connect the booster IC to a breadboard. The remaining components to the boost converter setup featured in Figure 10 were then connected to the breadboard.

The output of the boost converter was connected to the WID 3.0, which was monitored by an oscilloscope, and the power was provided by an adjustable DC power supply. Preliminary testing showed the boost converter circuit was capable of continuously powering the WID 3.0 for measurement and transmission with only an input voltage of 1.3V and current of 50mA. The output voltage signal is a distinct "saw-tooth" pattern, which is a result of the charging and discharging of the capacitors on the output voltage pin. Once a load is applied to the circuit (i.e. WID 3.0 wakes-up and operates), the output voltage signal is more stable with a central output voltage of 3V (Figure 11).

4. EXPERIMENTAL RESULTS

4.1 Piezoelectric Results

In order to optimize the voltage output of the various energy harvester configurations, the frequency of the base excitation should match the natural frequencies of the transfer function between output voltage and the base acceleration. The frequency response function of the L-shaped bracket (Figure 12) shows the first natural frequency of the beam around 2.7Hz and the second natural frequency around 7.5Hz. The poor coherence of the frequency response function below 20Hz corresponds with the significant amount of noise in the frequency response function itself, easily visible in the 0 – 160Hz plot. The experimental setup most likely generated this as the frequency response function is the linear average of 15 tests. The frequency response functions of all three of the harvester configurations illustrate the behavior of the natural frequencies as a tip mass is added to a cantilever and then when it is expanded into an L-shaped bracket:

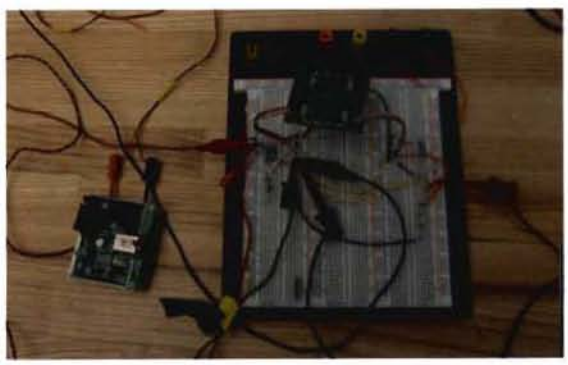

Figure 10: Boost Converter Test Setup

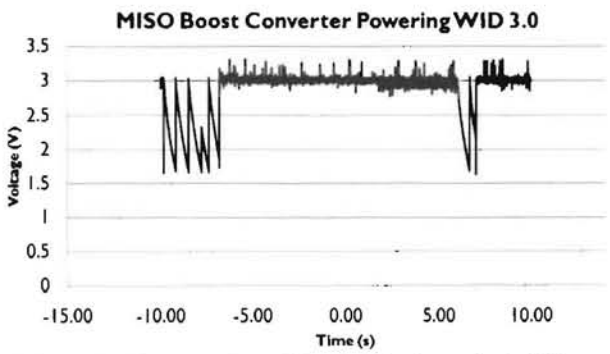

Figure 11: Output Voltage Signal while Powering WID3

Table 4: Frequency Response Function Results

Configuration	ω_1 (Hz)	ω_2 (Hz)	ω_2/ω_1
Cantilever	16	92	5.8
Cantilever w/Tip Mass	7.3	69	9.5
L-Shaped Bracket	2.7	7.5	2.8

From the normalized frequency response functions (Figure 13 & Table 4) of the three configurations in the frequency range of interest for the wind turbine blade, about 0-20Hz, it can be seen that the more mass added onto the end of the cantilever beam the lower the first natural frequency becomes, which is consistent with the theory. Also, the amount of damping in the system highly affects the response between the first and second natural frequencies of the L-shaped. Therefore a low amount of damping is necessary in the L-shaped bracket configuration.

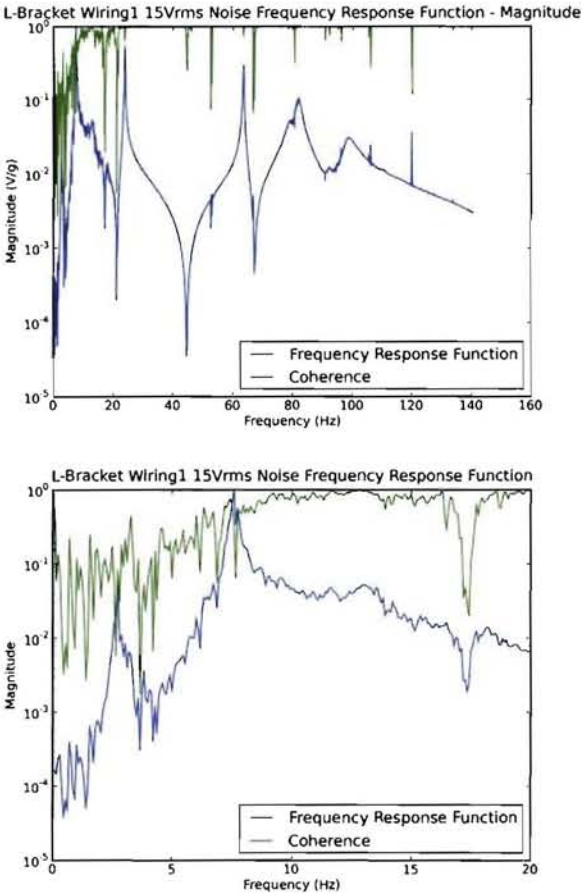

Figure 12: Normalized FRFs for L-Shaped Bracket

Next, it was verified that all three harvester configurations would be able to reach the output voltage levels necessary to charge the capacitor for the WID 3.0 sensor node to operate. All three of the configurations obtained the necessary 2.7V output at relatively small excitation accelerations and most did or could obtain the 3.5V maximum (Table 5). Capacitor charging tests (Figure 14) performed at both the first and second natural frequencies used a single frequency harmonic waveform excitation. A 1mF capacitor provided the most appropriate comparison between the three configurations based on the WID 3.0 power requirements as well as the performance of the configurations themselves. The tests lacking an rms base acceleration value used a lower measurement rate in order to increase the length of the test and therefore the resolution was not high enough to produce an accurate measurement. Also, the time values in Table 6 denoted with an asterisk indicate tests where the voltage across the capacitor peaked below the goal of 3.5 volts.

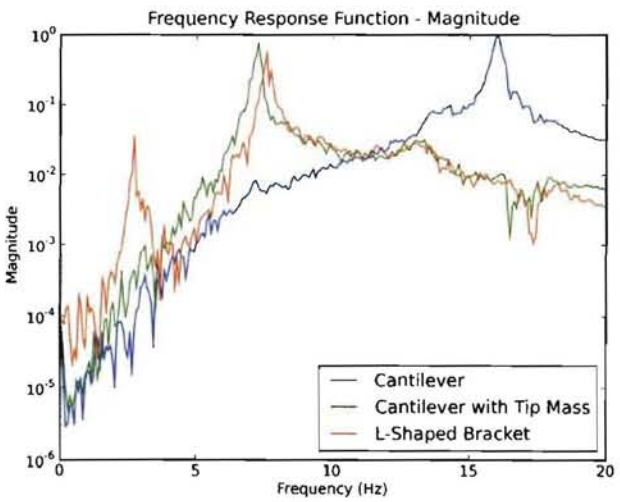

Figure 13: Normalized FRF Comparison

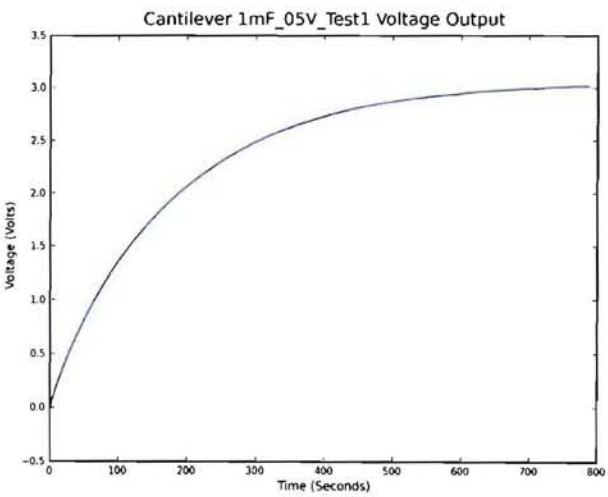

Figure 14: 1mF Cantilever Capacitor Charging Test

From Table 6, there is a consistent trend where as the frequency of excitation decreases, the ability of the harvester to charge the capacitor lowers as well. Also, the amount of base excitation required to charge the capacitor increases as the overall mass of the system increases, especially with the transition to the L-shaped bracket harvester configuration. Optimizing the design of the L-shaped structure to significantly decrease the mass would dramatically increase the output of the piezoceramic patches.

Table 5: Straight and Rectified Output Voltage Tests

Configuration	Excitation Voltage (V)	Freq. (Hz)	Voltage Condition	$A_{B,RMS}$ (g)	V_{max} (V)
Cant.	0.25	16.0	Straight	0.004	4.5
Cant.	0.25	16.0	Rectified	0.004	6.7
Cant.	1.00	92.0	Straight	0.087	4.1
Cant.	1.00	92.0	Rectified	0.086	7.4
w/Tip Mass	0.75	7.3	Straight	0.006	3.8
w/Tip Mass	0.75	7.3	Rectified	0.006	5.1
w/Tip Mass	0.50	69.0	Straight	0.012	3.5
w/Tip Mass	0.50	69.0	Rectified	0.013	6.2
L-Bracket	0.50	2.7	Straight	0.003	3.3
L-Bracket	0.50	2.7	Rectified	0.002	3.3
L-Bracket	0.25	7.5	Straight	0.003	3.2
L-Bracket	0.25	7.5	Rectified	0.003	3.1

Another issue of concern comes from the difference in the mode shapes between the first and second natural frequencies. As mentioned in Erturk et al[11], one wiring configuration cancellation occurs between the voltage outputs of the two piezoelectric patches in the first frequency, and the other wiring configuration cancellation occurs in the second frequency. Comparing the frequency response functions between the two different wiring configurations shows only small changes in magnitude of the system response for either frequency (Figure 15).

Also, tests using a dual-frequency excitation function targeting both the first and the second natural frequencies performed on the L-shaped bracket harvester explored the possibility of amplifying the voltage output of the energy harvester by coupling the first two modes. The results showed no change when the phase shift between the two frequencies varied between 0 and 90 degrees (Figure 16).

Table 6: 1mF Capacitor Charging Tests

Configuration	Freq. (Hz)	Excitation Voltage (V)	RMS Base Accel. (g)	Max Output Voltage (V)	Time (s)
Cant.	16.0	0.5	0.007	3.5	350
Cant.	16.0	1.0	0.016	3.5	160
Cant.	92.0	0.5	N/A	3.0	800*
Cant.	92.0	0.75	N/A	3.5	300
w/Tip Mass	7.3	1.5	0.012	3.2	1300*
w/Tip Mass	69.0	0.5	N/A	3.5	300
w/Tip Mass	69.0	1.0	N/A	3.5	90
L-Bracket	2.7	7.0	0.021	1.0	1000
L-Bracket	7.5	7.0	0.063	1.9	150*

4.2 Photovoltaic Results

As the temperatures of the PV cells and the mounting surface increased, a marginal increase in the output power from the cells resulted and can reasonably be attributed to the rising of the sun in the sky and decreasing solar incidence angle. There were large temperature variations on each individual cell and this was seen for all cells. The temperature of

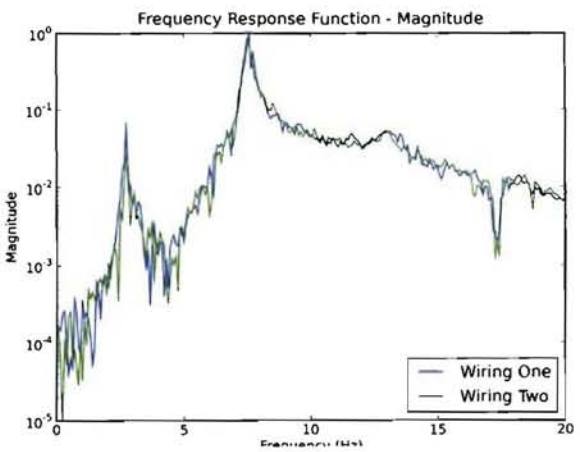

Figure 15: L-Shaped Bracket Wiring Comparison

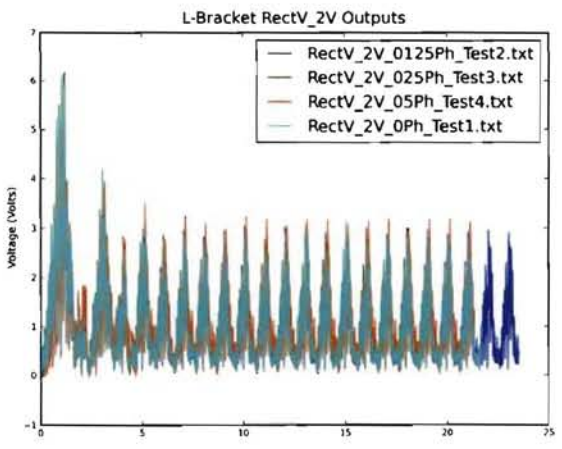

Figure 16: Dual Frequency Excitation Phase Variation.

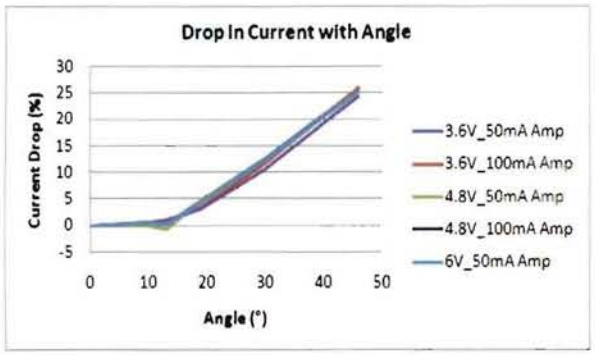

Figure 22: Percentage drop in current from initial value

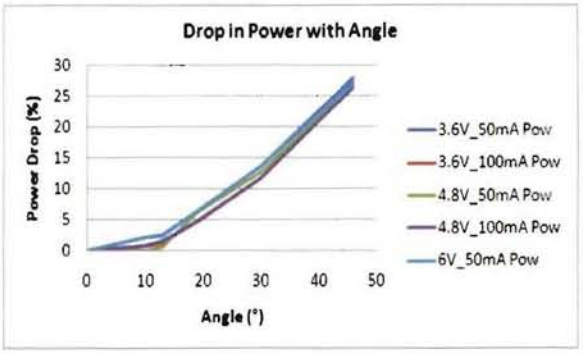

Figure 23: Percentage drop in power from initial value

the surface matched the temperature of the cells according to the thermocouple reading. However, when the surface temperature was measured using the IR thermometer, it was measured as 10°F less than what the thermocouple was reading.

As the solar incidence angle increased, the current and power of all the cells decreased. Overall the voltage did not drop noticeably from 0° to 46°, only decreasing by 2%. Drops in the current and power were not seen until after the 13° angle measurement. From the 13° angle measurement, the percentage drops in the current and power for all of the cells followed a linear pattern as can be seen in Figures 20 and 21. The overall percentage drop in current is about 25% and the overall percentage drop in power is about 27%. Increasing the solar incidence angle to a 45° angle has little effect on the voltage of our photovoltaic cells, but significantly decreases current and power. The condition with the solar incidence angle of 43° had similar results to the 46° angle discussed previously. The power of the cells placed in the sun at a solar incidence angle of 0°was the highest of the four environments. The power values were still in the hundreds of mW range for the 43° angle, but were about 32% less than the 0° angle. Although dependent on the voltage and current capacity of the cell, all of the power values were in the hundreds of milliwatts.

When the cells were placed in the lab with the fluorescent lights, little to no power was recorded. The exact solar radiation in the lab was not known, but it is probably the lowest of the five environments. A box with holes to let in light was the other low solar radiation condition. Similar values for power were seen in this condition although there was current present in every cell. The measurements taken when the cells were in the shade showed power in the range of tens of mW. In the shade, the voltage dropped by 40% and the current dropped to about 2 mA for the 50 mA cells and 5 mA for the 100 mA cells. Higher solar radiation conditions produced more power for the same cells, but there is still power available in conditions with lower solar radiation including shade. However, some amount of sunlight must be present to produce a usable level of power.

The power density delivered by the 100 mA cells to the 2.2F 2.5V capacitor was higher than the power density delivered by the 50 mA cells; the power density was calculated from the slope of the fitted line of the energy density curve (Figure 22). The largest power density seen was 1.67 mW/cm^2 in the 4.8V 100mA and the lowest power

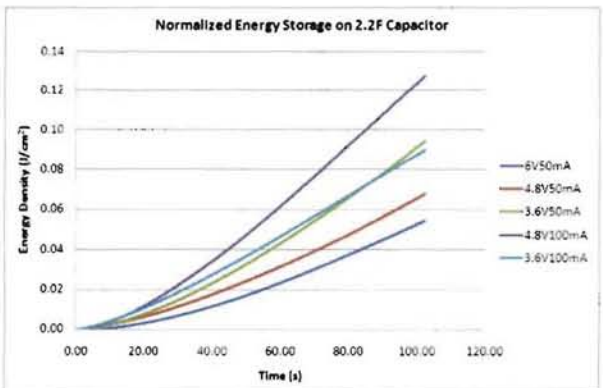

Figure 22: Energy density stored to 2.2F capacitor. Power density is represented by the slope.

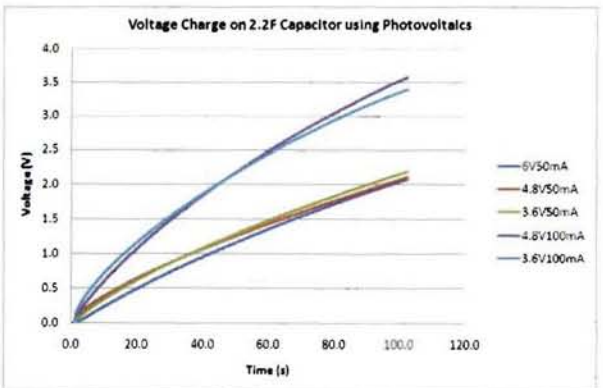

Figure 23: Voltage charged to 2.2F capacitor for different cells

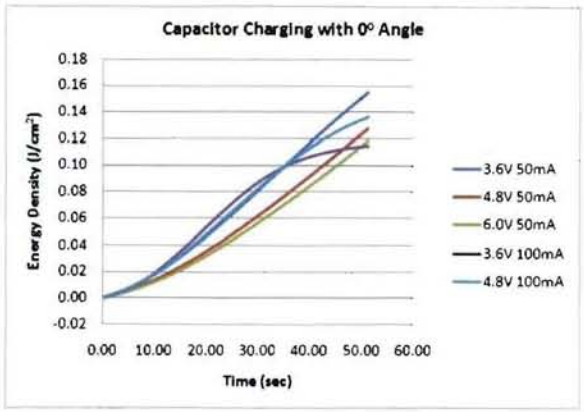

Figure 24: Energy density with 0° incidence angle.

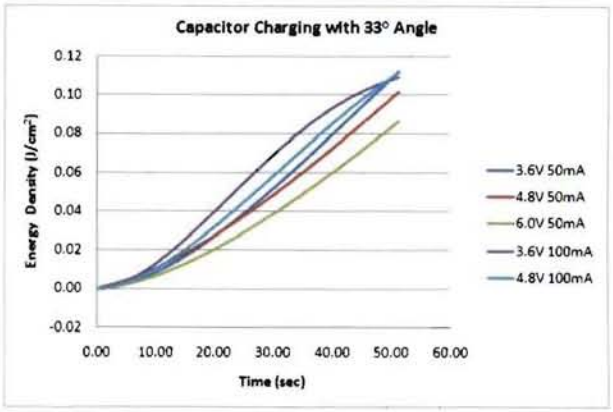

Figure 25: Energy density with 33° incidence angle.

density seen was 0.75 mW/cm^2 in the 6V 50mA. The power densities for the 3.6V cells were approximately the same for both current ratings. Over the span of 100 seconds, the capacitor was charged to 3.5 V with the 100 mA cells and 2 V with the 50 mA cells (Figure 23). The 4.8V 50mA cell produced the largest power density, but the power densities for all of the cells were in a very close range.

For the charging tests performed with solar incidence angles of 0° and 33°, the average difference in the power densities oscillated around zero after 40 seconds. Plots of the energy densities for both conditions (Figures 24 and 25) and the plot of the average power density difference are shown(Figure 26). The largest power density seen for the 33° angle condition was 2.8 mW/cm^2 in the 3.6V 100mA cell. The largest power density seen for the 0° angle was 3.5 mW/cm^2 in the 3.6V 100mA cell, which is quite a large difference from the 33° angle. However, when looking at the average power density difference plot, a 0.7 mW/cm^2 difference is the maximum value and after 40 seconds the average difference is approximately zero, which shows that the capacitor has reached full charge at this time.

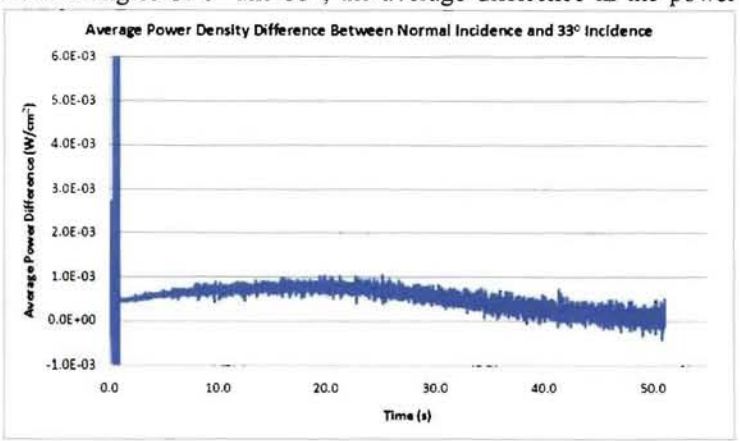

Figure 26: Average difference in power density for 0° and 33° Incidence angles.

5. SUMMARY AND CONCLUSIONS

The goal of this investigation has been to examine the feasibility of using different energy harvesting approaches to power embedded sensing hardware that could be used to interrogate the operational state and health of wind turbine blades. The three harvesting devices initially considered in this study include piezoelectric elements, thermoelectric modules, and photovoltaic cells. Of these three harvesters, the photovoltaic system was able to scavenge the most energy, as expected, due to the high energy density (per unit area) associated with the photovoltaic cells. The piezoelectric system used in this study was based upon an L-shaped bracket design that capitalizes on the nonlinear interaction between each leg of the bracket to reduce the spacing between the 1st and 2nd resonant modes to a theoretical limit of 2. Such spacing is advantageous in this application as some experimental turbine blades have demonstrated a harmonic response in the 1st and 2nd transverse modes, generating a kinetic environment that could be capitalized on by the L-shaped energy harvester. Lab tests indicated that a spacing of 2.78 could be obtained for the test structure used in this study. Further tests indicated that the hardware was capable of generating enough energy to power the wireless sensor node; however the time required was considerably longer than that of the photovoltaic cells. The final harvesting approach was the use of thermoelectric modules to capitalize on the thermal gradients that have been observed across the thickness of the wind turbine blades. Tests indicated that ~ 10°C could be expected across the blade thickness; however this was not sufficient to produce the power needed to operate one

of the WID sensor nodes. To address this issue a multi-input, single-output power conditioning circuit was developed to control how the power that is generated by each harvester is conditioned prior to being released to the sensor node. The circuit also has an integrated boost converter that allows the system to provide a 3.3V output given an input as low as 1.2V. Bench tests have shown that the system operates as intended, however further tests will be conducted to actually integrate the full suite of energy harvesters into one power supply system.

The result of this study is that a multi-source energy harvesting system has been demonstrated to be a feasible solution to the energy needs of wireless sensor nodes embedded within wind turbine blades. This is particularly true for photovoltaic and piezoelectric devices which can each generate the energy necessary to operate nodes such as the WID 3.0 sensor node. While each system has the potential to power the sensor node independently, a MISO power conditioning circuit will allow multiple harvesters to be used to power a single sensor node, providing a more robust power solution that would allow the integration of several transducers, such as thermoelectrics, to provide supplemental energy that could augment performance when direct solar or kinetic energy is not readily available. The proof of concept has been demonstrated in this initial study, and further development and testing of the MISO power conditioning circuit should result in a multi-source energy harvesting solution that will be integrated within test blades that are currently being proposed for field tests on a 19.8m wind turbine. The proposed test blades are currently scheduled to be flown in late 2011 / early 2012 at the U.S. Department of Agriculture – Sandia National Laboratory Wind Energy Technology Test Site near Amarillo, Texas.

REFERENCES

1. American Wind Energy Association, Annual Wind Energy Report Year Ending 2008, Annual Statistics on U.S. Wind Energy, January 2009. http://www.awea.org/publications/reports/AWEA-Annual-Wind-Report-2009.pdf
2. U.S. Department of Energy, Landowners' Frequently Asked Questions about Wind Development, August 2003. http://www.windpoweringamerica.gov/pdfs/wpa/34600_landowners_faq.pdf
3. Danish Wind Industry Association, Operation and Maintenance Costs for Wind Turbines, May 2003. http://www.windpower.org/EN/tour/econ/oandm.htm
4. Park, G., Farrar, C.R., Todd, M.D., Hodgkiss, W. & Rosing, T., "Energy Harvesting for Structural Health Monitoring Sensor Netorwks," Los Alamos National Labs Workshop, www.lanl.gov/projects/ei/pdf_files/LA-14314-MS.pdf, 2007.
5. Farinholt, K.M., Taylor, S.G., Overly, T.G., Park, G. & Farrar, C.R., "Recent Advances in Impedance-based Wireless Sensor Nodes," Proceedings of the ASME Conference on Smart Materials, Adaptive Structures and Intelligent Systems, 2008.
8. Sodano, H.A., Inman, D.J. & Park, G., "A Review of Power Harvesting from Vibration using Piezoelectric Materials," *The Shock and Vibration Digest*, **36**(3) pp. 197-205.
9. J.A. Paradiso and T. Starner, 2005, "Energy Scavenging for Mobile and Wireless Electronics," *IEEE Pervasive Computing*, **4**, pp.18–27.
10. U.S. Department of Energy, The Photoelectric Effect, Solar Energy Technologies Program, July 2009. http://www1.eere.energy.gov/solar/photoelectric_effect.html
11. A. Erturk, J. M. Renno, and D. J. Inman, "Piezoelectric Energy Harvesting from an L-Shaped Beam-Mass Structure," in *Proceedings of SPIE Conference on Active and Passive Smart Structures and Integrated Systems*, (San Diego, CA), 2008.
12. H. A. Sodano et al, "Recharging Batteries using Energy Harvested from Thermal Gradients," in *Journal of Intelligent Material Systems and Structures*, Vol. 18, Jan. 2007.